Nuclear Instruments and Methods in Physics Research A 1082 (2026) 170972

Contents lists available at ScienceDirect

Nuclear Inst. and Methods in Physics Research, A

journal homepage: www.elsevier.com/locate/nima

Full Length Article

Charge calibration of MALTA2, a radiation hard depleted monolithic active pixel sensor

Lucian Fasselt [a,b,*], Ignacio Asensi Tortajada [c], Prafulla Behera [d], Dumitru Vlad Berlea [a,b], Daniela Bortoletto [e], Craig Buttar [f], Valerio Dao [g], Ganapati Dash [d], Leyre Flores Sanz de Acedo [c], Martin Gazi [e], Laura Gonella [h], Vicente González [i], Sebastian Haberl [c], Tomohiro Inada [c], Pranati Jana [d], Long Li [j], Heinz Pernegger [c], Petra Riedler [c], Walter Snoeys [c], Carlos Solans Sánchez [c], Milou van Rijnbach [c], Marcos Vázquez Núñez [c,i], Anusree Vijay [d], Julian Weick [c], Steven Worm [a,b]

[a] Deutsches Elektronen-Synchrotron DESY, Zeuthen, Germany
[b] Humboldt University of Berlin, Berlin, Germany
[c] CERN, Geneva, Switzerland
[d] Indian Institute of Technology Madras, Chennai, India
[e] University of Oxford, Oxford, UK
[f] University of Glasgow, Glasgow, UK
[g] Stony Brook University, New Yorck, United States of America
[h] Università degli Studi di Trieste, Trieste, Italy
[i] Universitat de València, Valencia, Spain
[j] University of Birmingham, Birmingham, UK

ARTICLE INFO

Keywords:
DMAPS
Charge calibration
Tracking
High-energy physics

ABSTRACT

MALTA2 is a depleted monolithic active pixel sensor (DMAPS) designed for tracking at high rates and typically low detection threshold of 200 e^-. Threshold calibration is crucial to understanding the charge collection in the pixel. A simple procedure is developed to calibrate the threshold to unit electrons making use of a dedicated charge injection circuit and an Fe-55 source with dominant charge deposition of 1611 e^-. The injection voltage corresponding to the signal under exposure of Fe-55 is determined and serves as the basis for charge calibration. The charge injection circuit incorporates a capacitance with design value of $C_{inj} = 230$ aF. Experimentally, the average capacitance value for non-irradiated samples is found to be $C_{inj,exp} = 255 \pm 35$ aF and varies between sensors by 14% in terms of standard deviation. The deviation from the design value as well as among sensors motivates the need for the presented calibration procedure, which is proposed to be performed for each MALTA2 sensor and reduces the uncertainty down to 3% depending on the sensor.

1. Introduction

MALTA2 is the second generation of prototypes of the MALTA family of depleted monolithic active pixel sensors (DMAPS) designed in Tower 180 nm CMOS imaging sensor technology [1–3]. The MALTA2 pixel, with a pitch of 36.4 µm, consists of either high resistivity epitaxial or Czochralski silicon. The front-end in every pixel is optimized for threshold settings down to 200 e^- for detection efficiencies above 99%, as demonstrated for charged hadron beams [4]. Every pixel is equipped with a dedicated charge injection circuit (Fig. 1). It makes use of two voltage settings V_{HIGH} and V_{LOW} and a V_{PULSE} signal. A single pixel is selected through row and column selection bits. On the rising edge of V_{PULSE}, transistor M10 is switched off and M11 is switched on, so the output signal is a negative voltage step with an amplitude of $V_{HIGH} - V_{LOW}$. The resulting voltage difference is capacitively coupled to the input node of the front-end through a metal-to-metal connection that has a capacitance extracted from simulation of $C_{inj} = 230$ aF [5]. The injected charge is negative and has an absolute value of

$$Q_{inj} = C_{inj}\,\Delta V = C_{inj}(V_{HIGH} - V_{LOW}) \quad (1)$$

which assumes that the sensor capacitance of around 5 fF is large compared to the injection capacitance.

* Corresponding author at: Deutsches Elektronen-Synchrotron DESY, Zeuthen, Germany.
E-mail address: lucian.fasselt@desy.de (L. Fasselt).

https://doi.org/10.1016/j.nima.2025.170972
Received 11 February 2025; Received in revised form 14 August 2025; Accepted 17 August 2025
Available online 11 September 2025

This document describes the procedure to measure the capacitance of the charge injection circuit of MALTA2 assuming a linear behavior of the injected charge with respect to the difference of the V_{HIGH} and V_{LOW} voltages. ΔV_{Fe55} is the voltage difference that injects the same signal as an Fe-55 source. It is assumed that the charge deposited by the 5.9 keV K_α-line of an Fe-55 source is 1611 e^- [6].

X-rays are commonly selected for silicon sensors as calibration reference because of their point-like charge deposition. Charge calibration methods making use of X-rays and time-over-threshold (ToT) information include:

- **Radioactive sources** with discrete emission lines, such as Fe-55 (5.9 keV), Cd-109 (22.2 keV) and Am-241 (59.5 keV). For thin sensors of about 10 µm sensitive silicon, Fe-55 is typically selected due to its relatively low peak energy compared to other gamma sources [7]. Its K_α energy corresponds to the most probable energy deposition of a minimum-ionizing particle in 27 µm of silicon [8].
- **X-ray fluorescence** generated by irradiating secondary metal targets with a tungsten X-ray tube. Common targets and their K_α-lines include Fe (6.4 keV), Cu (8.0 keV), Mo (17.5 keV) and Cd (23.2 keV) [6,9]. This method allows adjustable flux and safe beam shutdown, though it requires access to an X-ray tube and monitoring of flux stability for reproducible energy spectra.
- **Compton scattering** of high-energy X-rays, for example from Am-241 (59.5 keV), where the scattered photon is reconstructed by a spectrometer on a swinging arm, while the recoil electron deposits a well-defined energy for each scattering angle in the silicon sensor [10]. This technique enables calibration down to about 1 keV but is limited by low statistics and poorer energy resolution compared to monoenergetic lines, making it unsuitable for routine calibration of large sensor batches.

For binary readout architectures, these calibration methods require longer measurement times, as the signal amplitude must be reconstructed from hit data [11,12]. A calibrated charge-injection circuit offers the advantage of compensating for changes in front-end settings, avoiding the need to repeat X-ray calibration after each configuration change. The injection capacitance calibration using X-ray sources has already been documented for sensors using ToT readout: For a hybrid pixel design using the FE-I4B integrated circuit produced in a 130 nm CMOS process an 18% larger injection capacitance of 6.7 fF is observed than expected from simulation [13]. The measurement is presented for a single chip and pixels are of the size of 250×50 μ^2m. For the monolithic FASTPIX sensor produced in 180 nm CMOS technology the calibration of the injection capacitance is performed based on two test pixels per chip and finds an approximately 60% higher value than the one extracted from simulation [14,15]. The effective capacitance is observed to increase for a larger pixel pitch. The capacitance determination presented here for MALTA2 is based on a purely digital readout using all pixels of the matrix. Variations between sensors are quantified. Also, the effect of non-ionizing energy loss (NIEL) is presented. In the following, the injected signals are quantified by the amplitude of the signal obtained through dedicated threshold scans, and ΔV_{Fe55} will be measured by dedicated source scans.

2. Methods

This chapter presents the methods used to calibrate a silicon sensor using X-ray data from digital readout. Section 2.1 introduces the functional principles of the MALTA2 front-end circuit, with a focus on the key DACs responsible for setting the discriminator threshold. Section 2.2 investigates the voltage input to the charge injection circuit, and Section 2.3 identifies their operational boundaries for reliable charge injection while explaining the reconstruction of amplitudes from digital injection data. Finally, Section 2.4 describes both the analog and digital response to an Fe-55 source, quantifying the amplitude of the main K_α-peak and its associated uncertainty, further discussed in Section 2.5.

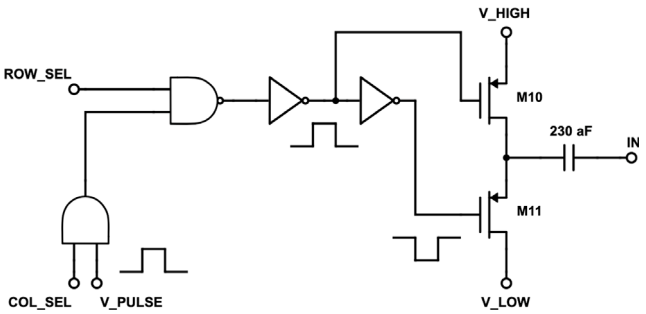

Fig. 1. MALTA2 charge injection circuit. The voltage step of $V_{HIGH} - V_{LOW}$ is capacitively coupled to the input of the front-end. The rise time of the front-end is about 30 ns and the recovery time 300 ns depending on the signal charge as well as the front-end biasing. The repetition rate of the injections is 10 kHz and limited by software. Consecutive injections in the same pixel are thus sufficiently separated by 0.1 ms [3,5].

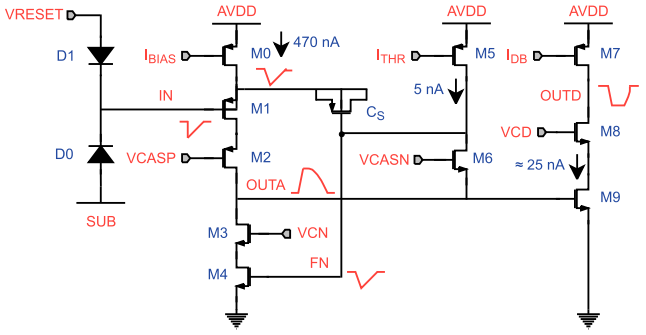

Fig. 2. MALTA2 front-end schematic including amplification, shaping and digitization of the analog signal per pixel [3]. IBIAS is the main biasing current and accounts for the majority of the power consumption. The current ITHR defines the speed of the feedback loop and is designed to effect the threshold of the discriminator.

2.1. MALTA2 front-end

A schematic of the MALTA2 front-end is shown in Fig. 2 and presented in more detail in [3]. The collection electrode is connected directly to the input node that is the gate of the transistor M1. M1 acts as a source follower biased by the current IBIAS which drives the gain as well as the power consumption of the front-end. Transistors M5 and M6 provide a low-frequency feedback and the bias voltage VCASN sets the DC voltage on OUTA. The current ITHR defines the speed of the return to baseline of OUTA after a particle hit and is suited to shift the detection threshold. A simple discriminator is formed by transistors M7 to M9.

2.2. Voltage measurement

The voltages V_{HIGH} and V_{LOW} are controlled by a DAC with a 7-bit range. The DAC value is set in a register which changes the voltage of a transistor. The voltage is copied to control pads with mirrors that are wire-bonded to a jumper on the PCB for monitoring. The voltage produced by the DAC as a function of the value of V_{HIGH}, as measured with a Keithley 2400, is shown in Fig. 3. A linear regime is observed from DAC value 0 to 90 with a gradient of 13.5 mV/DAC and an offset of 0.45 V. This value will be used to calculate the expected voltage of V_{HIGH}. The behavior of the V_{LOW} DAC is identical. For DAC values larger than 90 the voltage saturates due to a buffer stage which adds a voltage shift of 0.4 V and restricts the linear voltage generation. All DACs have been scanned for selected chips and the voltage generation of V_{HIGH} and V_{LOW} is understood to yield (13.5 ± 0.3) mV/DAC. This

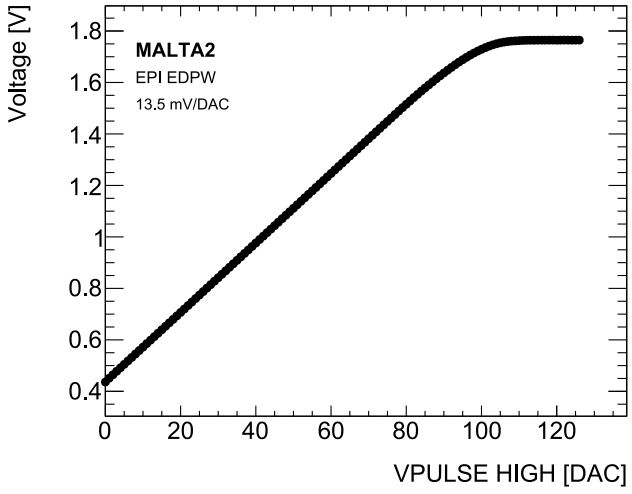

Fig. 3. V_{HIGH} voltage characteristic curve generated at the respective DAC value. The linear responds with a gradient of 13.5 mV/DAC holds up to a DAC value of 90.

measurement is not repeated for all chips but the uncertainty accounts for chip-to-chip variations. The current and voltage DACs have been measured after irradiation and show stable operation within the quoted uncertainty.

2.3. Digital amplitude of injected charge

A threshold scan is a variation of the ITHR current DAC that shifts the threshold set in the discriminator in the pixel front-end. It sets the pulse duration of the amplifier output. A higher value means a shorter signal and also a lower gain resulting in a higher charge threshold. The ITHR current determines how fast the signal returns to the baseline. Digital amplitude refers to the detection threshold, obtained via a threshold scan at constant injected charge, at which the probability of detecting a hit reaches 50%. Fig. 4(a) parameterizes the digital amplitude of charge injected into a single pixel through an s-curve

$$s(x; C, a, b) = \frac{C}{2}\left[1 - \mathrm{erf}\left(\frac{x-a}{\sqrt{2}b}\right)\right] \tag{2}$$

with the error-function definition

$$\mathrm{erf}\,(z) = \frac{2}{\sqrt{\pi}}\int_0^z \mathrm{e}^{-t^2}\,dt. \tag{3}$$

Its differentiation

$$\frac{d}{dx}s(x; C, a, b) = -C\,\mathcal{N}\left(a, b^2\right) \tag{4}$$

results in a Gaussian distribution with prefactor C, mean a and standard deviation b. 90% of the injected pulses are registered. This is an artifact of how the digital hits are handled at the end-of-column logic. The digital amplitude is quantified through the position parameter a of the error-function. The histogram of the digital amplitudes for all pixels in Fig. 4(b) is described by a Gaussian distribution with mean amplitude $\mu = 40.0$ and standard deviation $\sigma = 5.3$ that quantifies pixel-to-pixel variations.

According to Eq. (1), the injected charge ideally depends on $\Delta V = V_{HIGH} - V_{LOW}$ but not on the individual setting of the two DAC values. Consequently, a variation of V_{HIGH} and V_{LOW} should not affect the digital amplitude when keeping ΔV constant. Fig. 5 shows the mean digital amplitude as a function of V_{HIGH} and V_{LOW} while keeping ΔV constant at 10, 15, 20 and 25. A plateau forms for all ΔV which defines the range in which all injections yield a stable amplitude. The plateau is restricted towards large DAC values by $V_{HIGH} \leq 90$ and towards small DAC values by $V_{LOW} \geq 20$. Both restrictions are indicated by dashed lines. All amplitude deviations lie within ± 1.8 DAC units around the mean of the amplitudes inside the restricted region. Within this systematic uncertainty the amplitude does not depend on the specific value of V_{HIGH} or V_{LOW}. The restrictions are necessary because at low voltages the PMOS transistors that do switching between V_{HIGH} and V_{LOW} saturate and at high voltages the saturation, as discussed in Section 2.2, occurs. A reliable injection is obtained when keeping the DAC values within the range [20,90]. For this study low ΔV values give the best sensitivity as more pairs of $V_{HIGH} - V_{LOW}$ can be studied. The stable DAC range has also been verified in a low gain setting at reduced bias setting of IBIAS to be sensitive to larger ΔV values. The saturation effect of the injected charge does not depend on IBIAS. In summary, from the highest V_{HIGH} and lowest V_{LOW} setting follows a maximum injection at $\Delta V = 70$ DAC.

Table 1
Mn-55 X-ray emission lines with their corresponding energies and intensities [6]. The intensity is stated relative to the strongest line which is assigned the value 100.

Line	Energy [eV]	Intensity
$K_{\alpha,1}$	5898.8	100
$K_{\alpha,2}$	5887.6	50
K_{β}	6490.4	17

2.4. Digital amplitude of an Fe-55 signal

An X-ray source of Fe-55 is used commonly as a calibration source for thin silicon sensors because after its decay via electron capture to Mn-55 it emits X-rays at the transitions of the K_α-lines at 5.9 keV and K_β at 6.5 keV. The exact X-ray energies and intensities are listed in Table 1. An electron–hole pair creation energy in silicon of $\omega = (3.66 \pm 0.03)$ eV is assumed. The value was experimentally determined in [16] from the spectral responsivity of silicon photodiodes at room temperature, up to photon energies of 1.5 keV. It is consistent with measurements using 5.9 keV X-rays reported in [17] and with Monte Carlo simulations in [18]. Thus, the absorption of the K_α X-rays in silicon creates

$$N_e = 1611 \pm 13 \tag{5}$$

free electrons. The uncertainty on N_e includes the uncertainty in ω. The statistical fluctuation in charge generation characterized by the Fano factor $F \approx 0.12$ [17,19] is event-by-event about $14\,e^-$ and vanishes for the mean over sufficient events. The separation of the two K_α-lines, which is 11.1 eV corresponds to a generated charge of $3\,e^-$ and is negligible compared to the uncertainty on N_e.

Fig. 6 shows the analog spectra of two monitoring pixels from different MALTA2 sensors, one non-irradiated and one irradiated to 1×10^{15} 1 MeV $n_{eq}cm^{-2}$. The shape of both spectra is characterized by the K_α-peak, a less intensive K_β-peak and a flat tail towards small amplitudes due to charge sharing. The intensity ratio of the K_β to K_α contribution can be estimated by Gaussian fits to the experimental data and yield $10.8 \pm 3.7\%$ and $10.3 \pm 4.3\%$ for the non-irradiated and irradiated sample, respectively. The intensity ratio of the photon emission lines from Table 1 is 11.3% and falls within the statistical uncertainties of the experimental estimation. It is assumed as the ratio for data parameterization. The oscilloscope trigger level defines the cut-off at low amplitudes. The evident effect of the irradiation through non-ionizing energy loss (NIEL) is that of peak broadening and amplitude increase. Effective donor removal in the n-type implant reduces the pixel capacitance resulting in a larger amplitude [20]. The analog monitoring pixels are located at the edge of each sensor. For this work all pixels are to be included for calibration. Their digital readout through the MALTA2 front-end is designed for thresholds down to $200\,e^-$ to ensure high detection efficiency of minimum-ionizing particles [3]. As

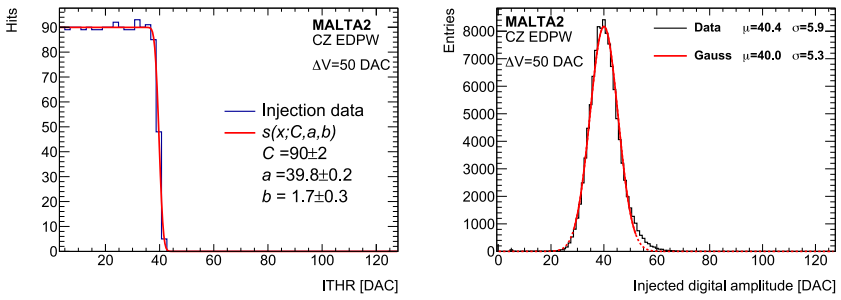

(a) Threshold scan of a single pixel under charge injection.

(b) Histogram of digital amplitudes for all pixels.

Fig. 4. The digital amplitude from charge injection with $\Delta V = V_{HIGH} - V_{LOW} = 50\,\text{DAC}$ is obtained in (a) for a single pixel through the position parameter a of an error-function fit with width b. The factor C scales with the number of injected pulses. As the threshold DAC current ITHR is raised above the injected signal the number of detected hits decreases. The histogram in (b) of digital amplitudes for all 224 × 512 pixels is described by a Gaussian fit to the core of the distribution. The stated values of the mean μ and the standard deviation σ are those calculated from the data or obtained through the fit.

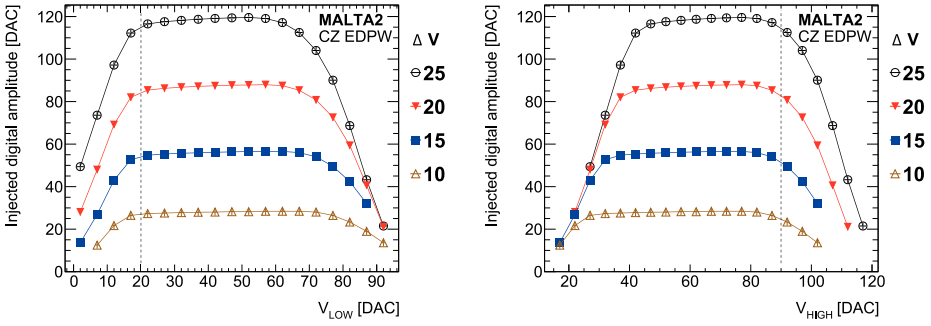

(a) Injected digital amplitude versus V_{LOW}.

(b) Injected digital amplitude versus V_{HIGH}.

Fig. 5. Injected digital amplitude versus V_{LOW} and V_{HIGH} for four different DAC settings of ΔV. The digital amplitude remains constant in a stable DAC range of [20,90]. The dashed lines mark the lower boundary for V_{LOW} and the upper boundary for V_{HIGH}. Outside that range, saturation effects reduce the injected charge which in turn causes a reduction in digital amplitude.

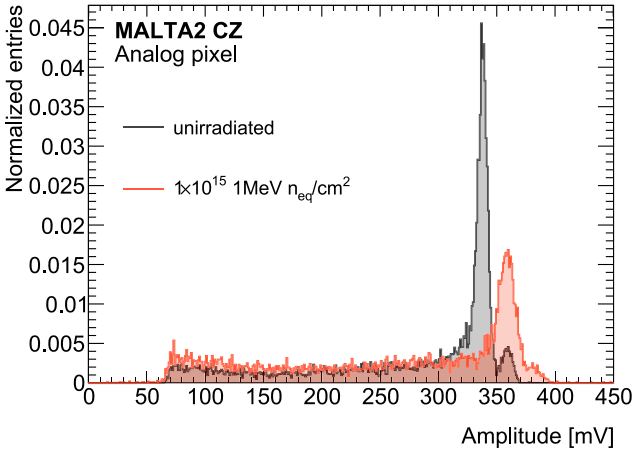

Fig. 6. Analog spectra of MALTA2 monitoring pixels exposed to an Fe-55 source. The prominent K_α-peak and the smaller K_β are separated even after irradiation. The flat tail at low amplitudes is due to charge sharing.

a result, the usual threshold range is far below the charge deposition of N_e. However, a low bias current setting in the front-end allows to suppress the gain and configure the threshold to values > 2000 e⁻. In such a low gain setting, a threshold scan over the charge range of an Fe-55 signal becomes possible. A threshold scan of all pixels of a MALTA2 sensor under exposure of an Fe-55 source is shown in Fig. 7(a). Only hits from single pixel clusters are selected. At this low gain setting two-pixel clusters make up less than 0.2% of the hits. They are unlikely because the detection threshold is large compared to the charge shared to neighboring pixels. The final threshold calibration (Fig. 9(b)) will show that already for ITHR set to 20 the threshold is about 1000 e⁻ and when reducing ITHR towards 0 there is an offset of about 700 e⁻. Additionally, the hit data is numerically differentiated so that a spectrum is obtained in Fig. 7(b) equivalent to that of the analog measurement. The underlying fit function is motivated by the analog measurement: The sum of two Gaussians $\mathcal{N}$ with mean values a_α and a_β correspond to the two X-ray peaks. The threshold smearing in terms of standard deviation b is assumed to be the same for both peaks. The height and area of the peaks are related by the theoretical intensities from Table 1. Finally, the flat tail towards low thresholds from charge losses is parameterized by an s-curve as defined in Eq. (2) with height n. It ends one standard deviation b before the signal peak to separate the tail from the peak. The fit function is defined as

$$\begin{aligned} f(x;c,a_\alpha,b,a_\beta,n) = \quad & c\,\mathcal{N}\left(a_\alpha, b^2\right) \\ & + \frac{17c}{150}\,\mathcal{N}\left(a_\beta, b^2\right) \\ & + s(x;n,a_\alpha - b, b) \end{aligned} \tag{6}$$

and its three contributions are visualized as dashed lines (see Fig. 7).

The digital hit measurement is sensitive to all charge depositions above a set threshold and is thus mathematically parameterized by the upper tail integral of Eq. (6) which yields

$$\begin{aligned} F(x;C,A_\alpha,B,A_\beta,N) = \quad & s(x;C,A_\alpha,B) \\ & + \frac{17}{150}s(x;C,A_\beta,B) \\ & + (A_\alpha - B - x)\,s(x;N,A_\alpha - B, B) \end{aligned} \tag{7}$$

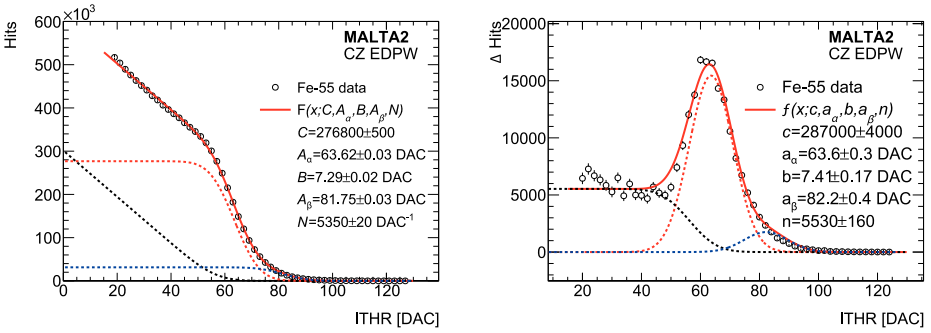

(a) Threshold scan data. (b) Differentiated data.

Fig. 7. Threshold scan under exposure of an Fe-55 source. Data points in (a) are the sum of hits from all pixels of a MALTA2 sensor. Only hits from single-pixel clusters are selected. (b) shows the numerically differentiated data, that is the difference between two data points. The fit functions $F(x)$ and $f(x)$ (solid red lines) consist of contributions from the K_α-peak (dashed red lines), the K_β-peak (dashed blue lines) and hits at lower thresholds from charge losses due to charge sharing (dashed black lines). The functions are defined in Eq. (6) and (7). The parameters A_α, a_α mark the position of the K_α peak and A_β, a_β that of K_β. B is the width of the falling edge of the s-curves and b the standard deviation of the Gaussian distributions. Both describe the threshold smearing due to pixel-to-pixel variations. The quoted uncertainties are statistical only. Systematic uncertainties are discussed in Section 2.5.

$$+\frac{N\,B}{\sqrt{2\pi}}\exp\left[-\left(\frac{A_\alpha - B - x}{\sqrt{2}B}\right)^2\right].$$

The first two s-curves arise as the integral of the Gaussian peaks and describe the K_α and K_β contributions. The charge sharing background is parameterized by a falling line that is smoothened out before reaching the baseline. The parameters from f and F are equivalent but labeled with small or capital letters, respectively. The two fits yield compatible results for the digital amplitude of $a_\alpha = 63.6 \pm 0.3$ DAC units, demonstrating the equivalence of fitting f to the differentiated data or F to the measured data. The statistical uncertainty on the fit parameters from f is larger than that of F and selected for further analysis. The width parameter $b = 7.4 \pm 0.2$ DAC units reflects pixel-to-pixel variations. This width estimation is compatible with the results from the injection scans, where the width from a single pixel is obtained as $b = 1.7 \pm 0.3$ DAC (Fig. 4(a)) and the main threshold smearing when summing all pixels is due to the threshold variation among pixels.

2.5. Uncertainty on digital Fe-55 signal

The reconstruction of the digital amplitude is performed for 6 non-irradiated MALTA2 sensors. The average absolute deviation between the results of A_α and a_α is found to be 0.2 DAC units while the maximum deviation among the six non-irradiated sensors is 0.4 DAC. This deviation is assumed as the systematic uncertainty on the amplitudes a_α which are used for the following charge calibration. The systematic uncertainty on a_β is estimated to be 2.2 DAC, approximately five times larger than that on a_α. The K_β-peak is modeled solely to improve the reconstruction accuracy of the main K_α-peak and is not used directly as an input for the calibration. The statistical fit uncertainty on the values of a_α are up to 1.1 DAC for samples with lower hit statistics than Fig. 7(a). This statistical component is combined in quadrature with the systematic uncertainty, and the resulting total uncertainty is used in subsequent error propagation. Table 2 summarizes all digital amplitudes a_α and threshold smearing b for different implantation doses of the n- implant. It shows that a higher doping of the n- layer leads to a reduced amplitude. This is explained by a larger pixel capacitance when increasing the n-type doping around the n^+ collection electrode as demonstrated in TCAD simulations [21]. A similar effect is discussed for the irradiated samples in Section 3.3.

3. Calibration results

3.1. Charge calibration through fe-55 source

Charge is injected for different values of ΔV and the mean digital amplitude is reconstructed according to the example for $\Delta V = 50$ in Fig. 4. The amplitude is found to be proportional to ΔV as shown in Fig. 8. The independently measured digital amplitude a_α under the exposure of the Fe-55 source is used as a charge calibration point. From the linear fit parameters m and y_0 the corresponding DAC value ΔV_{Fe55} is calculated as

$$\Delta V_{Fe55} = \frac{a_\alpha - y_0}{m} = 64.7 \pm 1.5\,. \tag{8}$$

The charge injected through the circuit at ΔV_{Fe55} yields the same amplitude as a_α. Further, the injection capacitance is calculated as

$$C_{inj} = \frac{1611\,e^- \times 1.602 \times^{-19} C/e^-}{\Delta V_{Fe55} \times 13.5\,mV/DAC} = \frac{19\,120\,aF}{\Delta V_{Fe55}/DAC} \tag{9}$$

by assuming a voltage input per unit ΔV in the injection circuit of 13.5±0.3 mV/DAC. It represents the average value across all pixels in a sensor.

Table 2 lists the calibration results of ΔV_{Fe55} and C_{inj} for all tested samples. Considering only the six non-irradiated samples an average

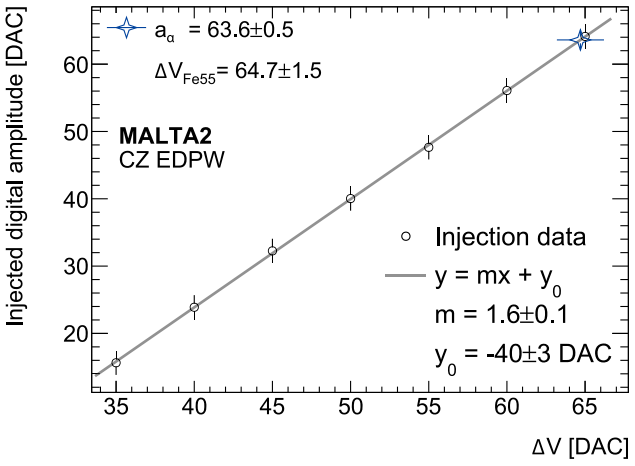

Fig. 8. Average digital amplitude versus injection DAC setting. Data points represent the mean from the Gaussian fit to all pixel amplitudes and the error bars represent the statistical uncertainty on the mean as well as the systematic uncertainty of 1.8 DAC units (Section 2.3). The digital amplitude a_{Fe55} from the Fe-55 detection is added as a calibration point to interpolate from the linear fit the corresponding charge injection ΔV_{Fe55} that yields the same digital amplitude.

Table 2
MALTA2 Calibration Results. Summarized is for each MALTA2 sample the implantation dose of the n-type implant underneath the electrode relative to the reference dose defined as 1. Very high refers to a 70% increased and low to a 23% decreased implantation dose compared to high. The absolute value of the doping concentration cannot be disclosed for NDA reasons. The irradiation fluence is quoted as non-ionizing energy loss (NIEL) in units of 10^{15} 1 MeV $n_{eq}cm^{-2}$. b is the threshold smearing that increases with irradiation. a_α is the digital amplitude from the K_α-X-rays from which the corresponding injection voltage ΔV_{Fe55} is interpolated. C_{inj} is the injection capacitance deduced according to Eq. (9).

sample	n- type implant dose	NIEL	a_α [DAC]	b [DAC]	ΔV_{Fe55} [DAC]	C_{inj} [aF]
W5R21	high (1.0)	0	66.3 ± 0.8	5.8 ± 0.4	77 ± 2	247 ± 10
W8R24	low (0.77)	0	91.9 ± 1.2	8.0 ± 1.0	88 ± 4	217 ± 11
W11R0	high (1.0)	0	63.6 ± 0.5	7.4 ± 0.2	64.7 ± 1.5	295 ± 10
W14R11	high (1.0)	0	60.4 ± 0.8	4.7 ± 0.4	86 ± 5	222 ± 14
W18R17	very-high (1.7)	0	44.3 ± 0.6	4.0 ± 0.3	75 ± 3	253 ± 12
W18R19	very-high (1.7)	0	38.8 ± 0.6	3.6 ± 0.3	64.2 ± 1.6	298 ± 11
W12R7	high (1.0)	1	77 ± 4	7.5 ± 0.7	79 ± 2	274 ± 11
W18R1	very-high (1.7)	1	52 ± 3	8.0 ± 0.5	69 ± 2	279 ± 11
W18R4	very-high (1.7)	2	74 ± 4	12.8 ± 1.6	60.8 ± 1.3	314 ± 10
W18R9	very-high (1.7)	3	63 ± 4	13.2 ± 1.5	49.1 ± 1.1	389 ± 13
W18R21	very-high (1.7)	3	74 ± 9	14 ± 6	54 ± 3	351 ± 20
W18R12	very-high (1.7)	5	83 ± 20	30 ± 16	46 ± 5	419 ± 51
W18R14	very-high (1.7)	5	84 ± 22	21 ± 13	43 ± 5	441 ± 55

injection capacitance of

$$C_{inj,exp} = 255 \pm 35\,aF \tag{10}$$

is found to be 11% larger than the design value of $C_{inj} = 230$ aF. For individual sensors the values span between 217 ± 11 aF and 298 ± 11 aF. Thus, some sensors show a significantly larger capacitance than the design value. For the Fe-55 equivalent injection DAC the average value is determined to be

$$\Delta V_{Fe55,exp} = 76 \pm 10\,DAC. \tag{11}$$

The stated uncertainties are the standard deviation of the sample and estimate the fluctuation among different sensors originating from the fabrication process. For sensors that have not been individually calibrated this value is assumed. The uncertainty on ΔV_{Fe55} however decreases from 10 DAC units down to uncertainties between 2 and 5 after individual sensor calibration as presented in Table 2. It is also the dominant uncertainty contribution to C_{inj}. Sensors with larger doping of the n-type implant show a decreased amplitude a_α due to a larger sensor capacitance. However, there is no significant effect on the calibration result of ΔV_{Fe55} because the injected amplitude also decreases. Even sensors with the same irradiation and doping from the W18 wafer show deviations of up to 15% which is the same order as the standard deviation across all non-irradiated sensors.

3.2. Calibrated threshold scans

Based on the result of ΔV_{Fe55} any charge injected into a MALTA2 sensor can be calibrated to unit electrons according to

$$Q_{inj} = \Delta V \frac{1611\,e^-}{\Delta V_{Fe55}}. \tag{12}$$

For a normal and low gain front-end setting the detection threshold is measured as an average over all pixels and is shown in Fig. 9. The low gain is the result of reducing the main front-end bias current IBIAS by a factor of 14 compared to the normal setting and leads to larger threshold values. All other DACs such as for example VCASN are kept constant. Any impact on the threshold of a change in DAC value would be measured during a threshold scan. The thresholds in unit electrons (left y-axes) are obtained through Eq. (12) based on the measurement of ΔV (right y-axes). Error bars quantify the statistical uncertainty on the mean threshold and are of the same order as the marker size. The threshold dependence on ITHR can be parameterized by a linear or quadratic function. These threshold values define the detection threshold at test beam studies and beam telescope applications [4,22,23]. The threshold resolution quantifying the standard deviation from pixel to pixel variations is around 10%. The systematic uncertainty contributions on the mean charge threshold are

- 0.8% from the reference number of electrons $N_e = 1611 \pm 13$ from the K_α-line due to the uncertainty in the electron–hole pair creation energy $\omega = (3.66 \pm 0.03)$ eV
- a sensor specific uncertainty on ΔV_{Fe55} that is between 2% and 6% for calibrated sensors. This uncertainty is dominated by the systematic uncertainty on the injected amplitude of 1.8 DAC which is propagated on to ΔV_{Fe55}. For uncalibrated sensors, where $\Delta V_{Fe55} = 76 \pm 10$ DAC, the uncertainty increases to 13% because no direct calibration is available and the average response from other calibrated sensors must be assumed instead.

3.3. Irradiation study

A selection of samples from the same wafer of 100 µm thick Czochralski silicon with increased doping of the n- layer has been neutron irradiated at different fluences of non-ionizing energy loss (NIEL) at the Triga reactor in the Institute Jožef Stefan (IJS), Slovenia. Table 2 shows that after irradiation the amplitude a_α as well as the threshold smearing b increase. This behavior has also been observed in the analog measurement of Fig. 6. The effect of irradiation is that the donor concentration in the n-type implant is effectively reduced, resulting in a decrease in pixel capacitance and thus an increase in amplitude [20,21].

The calibration results are compared in Fig. 10 and show a decrease in the Fe-55 equivalent injection voltage ΔV_{Fe55} with fluence. In irradiated samples, a lower injection voltage is needed to inject 1611 e^-. This can be qualitatively explained either due to charge trapping that leads to a reduction of collected charge from Fe-55 or due to an increase in the apparent injection capacitance from irradiation damage affecting the front-end. Two sensors are tested for each of the fluences at 1, 3 and 5×10^{15} 1 MeV $n_{eq}cm^{-2}$ and show compatibility within the stated 13% fluctuations as described above for non-irradiated sensors. The study shows that charge calibration has to account for the irradiation fluence for precise threshold determination to be able to compare thresholds among different irradiation levels.

4. Summary

The charge injection circuit of MALTA2 sensors has been calibrated inside a reliable DAC range of [20,90] for the parameters V_{HIGH} and V_{LOW}. A digital amplitude is reconstructed through threshold scans from binary hit data as the position parameter of an error-function fit. The amplitude is proportional to the voltage input of the charge injection circuit $\Delta V = V_{HIGH} - V_{LOW}$ and is calibrated through an Fe-55 source. Based on this, the charge injected into a MALTA2 sensor can be calculated via Eq. (12). The mean value of $\Delta V_{Fe55} = 76 \pm 10$ DAC is assumed for calibration of non-irradiated samples that are not calibrated individually. It is proposed that for calibration ΔV_{Fe55} is determined for each sensor to reduce the uncertainty from 13% to the 3% level depending on the sample. Neutron irradiated samples show a smaller value of ΔV_{Fe55} due to either a lower charge reference of Fe-55 due to charge trapping or an increase in the effective injection capacitance. Once the charge calibration parameter ΔV_{Fe55} is obtained, the threshold setting of a MALTA2 sensor is quantifiable at any front-end setting through charge injection. The described procedure is feasible for any binary sensor that incorporates an injection circuit.

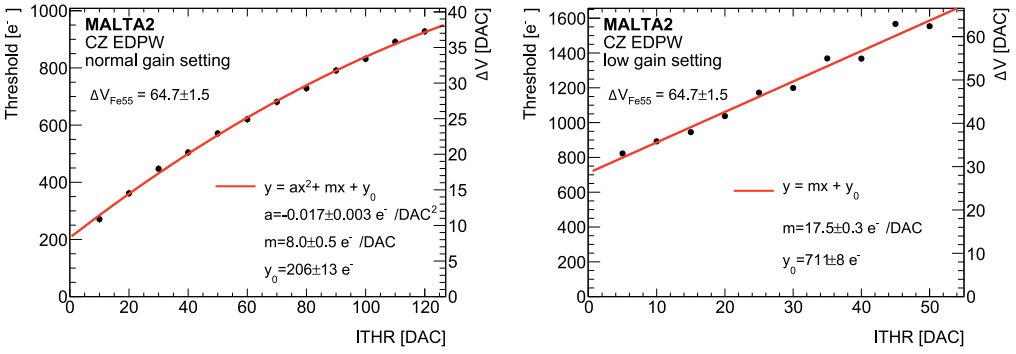

(a) Thresholds for front-end at normal gain. (b) Thresholds for front-end at low gain.

Fig. 9. Calibrated threshold as a function of the ITHR DAC. For each ITHR value, the threshold is measured per pixel in units of injected charge ΔV (right y-axes). The calibration input of ΔV_{Fe55} makes a linear calibration from ΔV to unit electrons according to Eq. (12) possible (left y-axes). (a) shows a normal gain setting at IBIAS = 43 with thresholds down to 200 e^- and a parabolic fit. (b) shows a low gain front-end setting at IBIAS = 3 with thresholds above 750 e^- and a linear fit.

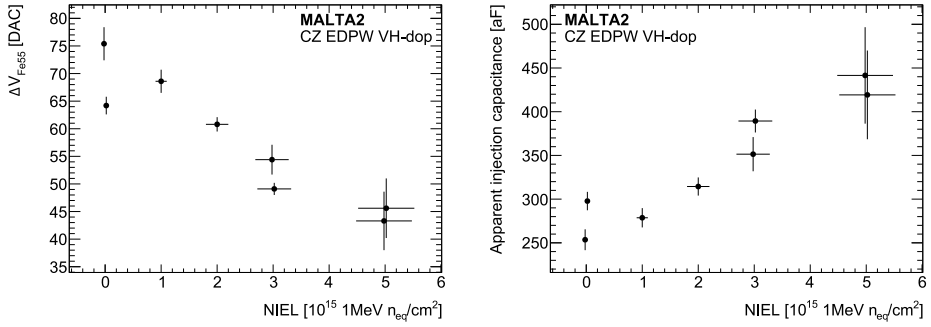

(a) ΔV_{Fe55} versus NIEL. (b) Apparent injection capacitance versus NIEL.

Fig. 10. Dependence of ΔV_{Fe55} (a) and the corresponding injection capacitance (b) on the irradiation fluence as non-ionizing energy loss (NIEL). All samples originate from the same wafer of 100 µm thick Czochralski silicon with increased doping of n- layer. ΔV_{Fe55} is the voltage DAC value that injects a charge of 1611 e^- corresponding to the main Fe-55 deposition. ΔV_{Fe55} decreases with irradiation. Consequently, the apparent injection capacitance increases with irradiation because a lower voltage is needed to inject the same reference charge.

CRediT authorship contribution statement

Lucian Fasselt: Writing – review & editing, Writing – original draft, Visualization, Software, Methodology, Investigation, Formal analysis. **Ignacio Asensi Tortajada:** Software, Investigation, Data curation. **Prafulla Behera:** Supervision, Funding acquisition. **Dumitru Vlad Berlea:** Software, Methodology, Investigation. **Daniela Bortoletto:** Supervision, Funding acquisition. **Craig Buttar:** Supervision, Funding acquisition. **Valerio Dao:** Supervision, Software. **Ganapati Dash:** Software, Investigation. **Leyre Flores Sanz de Acedo:** Software, Methodology. **Martin Gazi:** Software, Investigation. **Laura Gonella:** Supervision, Funding acquisition. **Vicente González:** Supervision, Funding acquisition. **Sebastian Haberl:** Software, Investigation. **Tomohiro Inada:** Software, Resources. **Pranati Jana:** Investigation. **Long Li:** Software, Investigation. **Heinz Pernegger:** Supervision, Funding acquisition, Conceptualization. **Petra Riedler:** Project administration, Funding acquisition. **Walter Snoeys:** Supervision, Funding acquisition. **Carlos Solans Sánchez:** Writing – review & editing, Supervision, Software, Resources, Project administration, Methodology, Funding acquisition, Conceptualization. **Milou van Rijnbach:** Writing – review & editing, Supervision, Software, Methodology. **Marcos Vázquez Núñez:** Resources, Investigation. **Anusree Vijay:** Software, Investigation. **Julian Weick:** Software, Resources. **Steven Worm:** Supervision, Resources, Methodology, Funding acquisition.

Declaration of competing interest

The authors declare that they have no known competing financial interests or personal relationships that could have appeared to influence the work reported in this paper.

Acknowledgments

This project has received funding from the European Union's Horizon 2020 Research and Innovation programme under Grant Agreement number 101004761 (AIDAinnova), and number 654168 (IJS, Ljubljana, Slovenia). Furthermore it has been supported by the Marie Sklodowska-Curie Innovative Training Network of the European Commission Horizon 2020 Programme under contract number 675587 (STREAM).

Data availability

Data will be made available on request.

References

[1] H. Pernegger, et al., First tests of a novel radiation hard CMOS sensor process for Depleted Monolithic Active Pixel Sensors, JINST 12 (06) (2017) P06008, http://dx.doi.org/10.1088/1748-0221/12/06/P06008.

[2] I. Berdalovic, et al., MALTA: a CMOS pixel sensor with asynchronous readout for the ATLAS High-Luminosity upgrade, in: Proc. IEEE Nucl. Sci. Symp. Med. Imag. Conf., 2018, 8824349, http://dx.doi.org/10.1109/NSSMIC.2018.8824349.

[3] F. Piro, et al., A 1 μW radiation-hard front-end in a 0.18 μm CMOS process for the MALTA2 monolithic sensor, IEEE Trans. Nucl. Sci. 69 (6) (2022) http://dx.doi.org/10.1109/TNS.2022.3170729.
[4] M. van Rijnbach, et al., Radiation hardness of MALTA2 monolithic CMOS imaging sensors on Czochralski substrates, Eur. Phys. J. C 84 (3) (2024) 251, http://dx.doi.org/10.1140/epjc/s10052-024-12601-3, arXiv:2308.13231.
[5] I. Berdalovic, Design of Radiation-Hard CMOS Sensors for Particle Detection Applications (Ph.D. thesis), Zagreb U., 2019.
[6] A. Thompson, et al., X-ray Data Booklet, second ed., Lawrence Berkeley National Laboratory, University of California, 2009, URL https://xdb.lbl.gov/xdb-new.pdf.
[7] G. Aglieri Rinella, et al., Characterization of analogue Monolithic Active Pixel Sensor test structures implemented in a 65 nm CMOS imaging process, NIMA 1069 (2024) 169896, http://dx.doi.org/10.1016/j.nima.2024.169896.
[8] S. Meroli, et al., Energy loss measurement for charged particles in very thin silicon layers, JINST 6 (06) (2011) P06013, http://dx.doi.org/10.1088/1748-0221/6/06/P06013.
[9] J. Jakubek, Precise energy calibration of pixel detector working in time-over-threshold mode, NIMA 633 (2011) S262–S266, http://dx.doi.org/10.1016/j.nima.2010.06.183, 11th International Workshop on Radiation Imaging Detectors (IWORID).
[10] P. McCormack, et al., New method for silicon sensor charge calibration using Compton scattering, 2020, arXiv:2008.11860.
[11] D.-L. Pohl, et al., Obtaining spectroscopic information with the ATLAS FE-I4 pixel readout chip, NIMA 788 (2015) 49–53, http://dx.doi.org/10.1016/j.nima.2015.03.067.
[12] L. Fasselt, et al., Energy calibration through X-ray absorption of the DECAL sensor, a monolithic active pixel sensor prototype for digital electromagnetic calorimetry and tracking, Front. Phys. 11 (2023) http://dx.doi.org/10.3389/fphy.2023.1231336.
[13] M. Backhaus, Characterization of new hybrid pixel module concepts for the ATLAS Insertable B-Layer upgrade, JINST 7 (01) (2012) C01050, http://dx.doi.org/10.1088/1748-0221/7/01/C01050.
[14] J. Braach, et al., Performance of the FASTPIX sub-nanosecond CMOS pixel sensor demonstrator, Instruments 6 (1) (2022) http://dx.doi.org/10.3390/instruments6010013.
[15] J. Braach, Performance Evaluation of the FASTPIX Silicon Pixel Sensor Technology Demonstrator for High-Precision Tracking and Timing (Ph.D. thesis), U. Hamburg (main), 2024-05-16, 2024, http://dx.doi.org/10.3204/PUBDB-2025-01037.
[16] F. Scholze, H. Rabus, G. Ulm, Mean energy required to produce an electron-hole pair in silicon for photons of energies between 50 and 1500 eV, J. Appl. Phys. 84 (1998) 2926–2939, URL https://api.semanticscholar.org/CorpusID:55814610.
[17] B. Lowe, R. Sareen, A measurement of the electron–hole pair creation energy and the Fano factor in silicon for 5.9keV X-rays and their temperature dependence in the range 80–270K, NIMA 576 (2) (2007) 367–370, http://dx.doi.org/10.1016/j.nima.2007.03.020.
[18] M. Mazziotta, Electron–hole pair creation energy and Fano factor temperature dependence in silicon, NIMA 584 (2) (2008) 436–439, http://dx.doi.org/10.1016/j.nima.2007.10.043.
[19] F. Perotti, C. Fiorini, Observed energy dependence of Fano factor in silicon at hard X-ray energies, NIMA 423 (2) (1999) 356–363, http://dx.doi.org/10.1016/S0168-9002(98)01264-9.
[20] H. Pernegger, et al., MALTA-Cz: a radiation hard full-size monolithic CMOS sensor with small electrodes on high-resistivity Czochralski substrate, JINST 18 (09) (2023) P09018, http://dx.doi.org/10.1088/1748-0221/18/09/P09018.
[21] K. Dort, Simulation Studies and Characterisation of Monolithic Silicon Pixel-Detector Prototypes for Future Collider Detectors & Unsupervised Anomaly Detection in Belle II Pixel-Detector Data (Ph.D. thesis), University of Giessen (Germany), 2022, URL https://cds.cern.ch/record/2813457.
[22] L. Fasselt, et al., Charge reconstruction from binary hit data on irradiated MALTA2 Czochralski sensors, NIMA 1080 (2025) 170747, http://dx.doi.org/10.1016/j.nima.2025.170747.
[23] G. Gustavino, et al., Development of the radiation-hard MALTA CMOS sensor for tracking applications, in: Proc. Vertex 2023, vol. 448, 2024, p. 048, http://dx.doi.org/10.22323/1.448.0048.